Nanoscopic Surface Decomposition of $Pr_{0.5}Ba_{0.5}CoO_{3-\delta}$ Perovskite Turns Performance Descriptors Ambiguous

David N. Mueller[1,2,*], Margret Giesen[1,*], Tomáš Duchoň[1,*], Stefan Cramm[1], Felix Gunkel[2], Matteo Jugovac[1,§], Giovanni Zamborlini[1,$], Vitaliy Feyer[1], Claus M. Schneider[1]

[1]Peter Grünberg Institute PGI-6, Forschungszentrum Jülich GmbH, 52425 Jülich, Germany

[2]Peter Grünberg Institute PGI-7, Forschungszentrum Jülich GmbH, 52425 Jülich, Germany

*dav.mueller@fz-juelich.de, m.giesen@fz-juelich.de, t.duchon@fz-juelich.de

[§]Present Address: Experimentelle Physik 6, Technische Universität Dortmund, Otto-Hahn-Str. 4, 44227 Dortmund, Germany

[$]Present Address: ELETTRA sincrotrone Trieste, s.s. 14 km 163,500 in Area Science Park, 34149 Basovizza TS, Italy

Keywords: perovskite, PBCO, transition metal oxide, Cahn-Hilliard, decomposition, principal component analysis, activity descriptor

Abstract

The surface electronic structure of a material is frequently used to identify simple descriptors for its catalytic efficacy and other properties. In order to harness the predictive ability of such descriptors, structural and chemical evolution of the material when exposed to operating conditions, such as oxidizing environment and high temperatures, need to be considered. These evolutions occur at length scales not easily observable, leading to an averaging over short-range variations and thus misinterpretation of the property in question. Here, we investigate the perovskite $Pr_{0.5}Ba_{0.5}CoO_{3-\delta}$ as a prototypical mixed ionic–electronic conductor that exhibits promising catalytic properties toward the oxygen evolution reaction in electrochemical cells, which have been characterized by such descriptors. We employ spatially resolved X-ray absorption spectroscopy and find a Cahn-Hilliard-type decomposition process at sub µm length scales after mere hours at operating or processing conditions. The observation is in contrast to the thermodynamic stability of the $Pr_{0.5}Ba_{0.5}CoO_{3-\delta}$ bulk, suggesting the decomposition to be confined to the surface. Our results showcase a considerable lateral inhomogeneity of the surface electronic structure, emphasizing that descriptors derived through spatially averaging techniques have to be heavily scrutinized.

Introduction

The need for cost-effective, highly active catalysts for electrochemical energy conversion has triggered a tremendous amount of research towards new materials. One thrust is the identification of structure–property relationships that would allow a simple prediction of catalytic efficacy from material properties. Activity descriptors from structure–property relationships have been found to work well in chemically and structurally simple metals[1] and their binary alloys[2,3] used as fuel cell catalysts. Later, the same descriptors have been proposed to work also for more complex materials such as perovskite-type oxides.[4]

The chemical versatility of the perovskite structure ABO_3 opens up pathways for elaborate substitution schemes on both A- (usually alkaline earth or lanthanide elements) and B-site (transition metals) to tune chemistry and electronic structure towards favorable properties. Candidates with superior activity towards the oxygen evolution (OER) and reduction reactions, factors limiting the efficiency of both high (solid oxide electrochemical cells, SOEC)[5,6] and room temperature (water splitting) applications, have been found.[7] Among others,[8] the filling of the e_g electronic states originating from the octahedral BO_6 building block was proposed to serve as an activity descriptor for water splitting efficacy,[4] with the e_g electrons later found to be the participating electronic species in high temperature redox processes.[9] Whether this (or any) simple descriptor works reasonably well to predict catalytic efficacy is a matter of debate which recently has been summarized and discussed extensively in a review paper by *Antipin* and *Risch*.[10] This work does not partake in the discussion, but rather aims to highlight the existence of experimental limitations that hamper identification and quantification of the descriptors even prior to drawing any connection to the activity.

Regardless of which physical or chemical property is used as a descriptor, rarely do complex oxide surfaces remain chemically and structurally unaltered at operating conditions in contrast to their monometallic counterparts. Already in the bulk, without the added complexity of the surface discontinuity, Gibb's phase rule dictates that the more components a material has, the more likely decomposition becomes, which sometimes can be counteracted by entropic stabilization at higher temperatures. In fact, the champion material for the oxygen evolution reaction that was supposedly identified through such descriptors, $(Ba,Sr)(Co,Fe)O_{3-\delta}$ (BSCF),[7] had, by that point, already been found to suffer from thermochemical instability resulting in bulk decomposition[11], the configuration entropy through mixed A- and B-site and unsurpassed oxygen vacancy concentration only managing to stabilize the cubic phase above feasible operating temperatures. The decomposition affects the physical properties, and, with that, any structure–property relationship that has been identified or tailored in the initial material.

Decompositions and chemical instabilities can be expected to become even more severe at the surface. Two common reasons for stoichiometric and structural changes at the surface are the segregation of cations and the precipitation of secondary phases.[12,13] Thin film model systems used to investigate catalytic processes are especially prone to these surface rearrangements due to their increased concentration of point defects[14] and their high surface to bulk ratio. These make the thin films inherently unstable, potentially rendering the decomposed surface under operating conditions far from the material that was supposed to be studied. Though *operando* techniques have been used extensively to observe catalyst materials in their operating environment, alleviating the disconnect between bulk chemistry and the rearranged surface,[15] here, we want to point out another—up to now largely overlooked—obstacle:

The processes that alter the surface structure and chemistry during operation are spatially heterogeneous in nature and thus require spatially non-averaging techniques,[16] such as spectromicroscopy, in order to be captured in their entirety. However, while separate spectroscopic and microscopic studies are abundant, as discussed, a proper spectrochemical study is missing. The ability to create thin films of high quality and flatness, though compounding decomposition and phase instabilities, makes observation of these processes on such length scales and with the techniques used in this work possible in the first place.

In this work, we report the particular case of $Pr_{0.5}Ba_{0.5}CoO_{3-\delta}$ (PBCO) thin films, one contender for an oxidic cathode material for both high[17] and low-temperature applications,[18–20] which we expose to typical SOEC operation and thin film processing conditions. We use X-ray photoemission electron microscopy (X-PEEM) in X-ray absorption (XAS) mode to determine the surface composition and electronic structure with high lateral resolution and find severe inhomogeneities akin to Cahn-Hilliard-type decomposition evolving at relatively short time scales. Consequently, any descriptors identified from the surface electronic structure will share the inhomogeneity.

Methods

Experimental

Highly oriented thin films of $Pr_{0.5}Ba_{0.5}CoO_{3-\delta}$ were deposited by pulsed laser deposition (PLD) at 1123 K on $NdGaO_3$ (100) oriented substrates as described elsewhere.[20] Crystallinity and formation of the cubic perovskite phase were confirmed by X-ray diffraction, and the thickness of the films was determined to be 44 nm by X-ray reflectivity measurements. Edge-to-edge resistance of the films was determined to be 1.5 kΩ, and thus no charging effects were observed in the PEEM. In the study presented here, we analyzed PBCO samples after three different annealing treatments: One sample was spectroscopically studied as-prepared without any further sample annealing. This sample is denoted as sample “ap”. Samples “2h” and “12h” were subject to 2h and 12h of annealing at 1073 K in a stagnant atmosphere of 200 mbar O_2, respectively. After annealing, both samples were quenched to room temperature in the pertaining atmosphere and immediately transferred to the microscope chamber without exposure to ambient atmosphere in order to avoid contamination with atmospheric reactants, such as H_2O and CO_2. We have summarized the annealing procedures covered in this study in Table S1 of the supporting information.

The X-PEEM experiments were carried out at the NanoESCA beamline of the ELETTRA synchrotron (Trieste, Italy) in partial electron yield, where the energy cutoff of detected electrons was set to 5 eV and at the UE56/1-SGM beamline of BESSY II (Berlin, Germany) in the total electron yield mode. Information depth of both techniques is estimated to be on the tens of nanometer scale. The individual experiments, including spectral ranges, are itemized in Table S1 in the supporting information. PEEM images obtained at ELETTRA have a square shape with a total size of 600 × 600 pixels encompassing a circular field of view (FoV) of 10 µm in diameter. The circular FoV contains 252448 pixels in total, with an image resolution of 18 nm per pixel. PEEM images recorded at BESSY II have a similar resolution per pixel with an image size of 688 × 520 pixels. The FoV contains 321814 pixels in total. The number of pixels in both cases equals the number of X-ray absorption spectra analyzed in this study. To make the observed surface features better visible to the reader, we show 180 × 180 pixel segments of the original PEEM images for all samples, corresponding to a sample area of $3.2 \times 3.2\ \mu m^2$. The areas are representative of the full FoV, with the full-sized images provided in the supporting information (Figures S1 and S2).

Multivariate methods for data analysis

We used two multivariate methods for data analysis: principal component analysis (PCA)[21] and ortho-non-negative matrix factorization (o-NNMF).[22] As exploratory data analysis methods, both are well suited to examine PEEM data where little is known about possible spectral correlations.

In PEEM, spectral information is given as measured intensity at distinct points in a 3-dimensional coordinate system spanned by two spatial axes (i.e. pixels per PEEM image) and one photon energy axis. Given a large pixel number per PEEM image (~100000s), manual data analysis is impractical. Though intensity maps at energies of characteristic spectral features and spectra at certain points (or regions of interest, ROI) can give qualitative information on inhomogeneities and their physicochemical nature, respectively, unbiased evaluation of the complete data set is difficult to achieve. PCA and o-NNMF overcome this limitation by using all spectra in the PEEM data set and guarantee an unbiased analysis by identifying all spectral variations and similarities, even if these are not perceptible by eye in the PEEM image.

PCA decomposes the spectra at each pixel into a linear combination of principal components (PCs). The PCs represent uncorrelated spectral variations and are oriented along the largest spectral variances (in PCA terminology called 'loadings'). As such, correlated variances in spectral features appear in the same loading, and uncorrelated spectral changes are covered by different loadings. If spectral variances related to changes in material properties are above the noise level, PCA incidentally separates the spectral signal from noise. The coefficients of the linear combination of PCs map their spatial distribution over the field of view of the PEEM data. Hence, the coefficients of a single PC allow us to visualize how much the PC contributes to the pixel intensity of the PEEM image. The mapping of individual PC loadings to the pixel intensity in the PEEM images has been extensively discussed for PBCO in our prior work.[23] In this work, we take advantage of PCA for the purpose of separation of actual data from experimental noise. To differentiate original PEEM images from the PCA treated, noise-reduced images, we call the latter "PCA images" in the following.

In order to automatically sort spectra into groups (‘clusters’) of high spectral similarity we employ o-NNMF. The spectra are averaged within the clusters. As we will see later, pixels in distinct clusters form connected areas and resemble the structures, as seen in the PEEM images. Hence, o-NNMF, as used here, replaces a manual definition of ROIs and is less prone to unintentionally biased data analysis.

The partial steps of the analysis are fully described in the supporting information, and we kindly refer the reader interested in the mathematical background to previous works.[23]

Results and Discussion

Evolution of spectra with annealing time

Figures 1a–c show X-ray absorption spectra spatially averaged over the entire FoV for samples ‘ap’ (bottom), ‘2h’ (center) and ‘12h’ (top curves) at the Oxygen K-, Cobalt $L_{3,2}$-, Barium $M_{5,4}$- and Praseodymium $M_{5,4}$-edges. PEEM images obtained at the energies corresponding to the features A through K are shown in Figure 1d. The assignment of the features to electronic transitions and their henceforth used designations are summarized in Table 1.

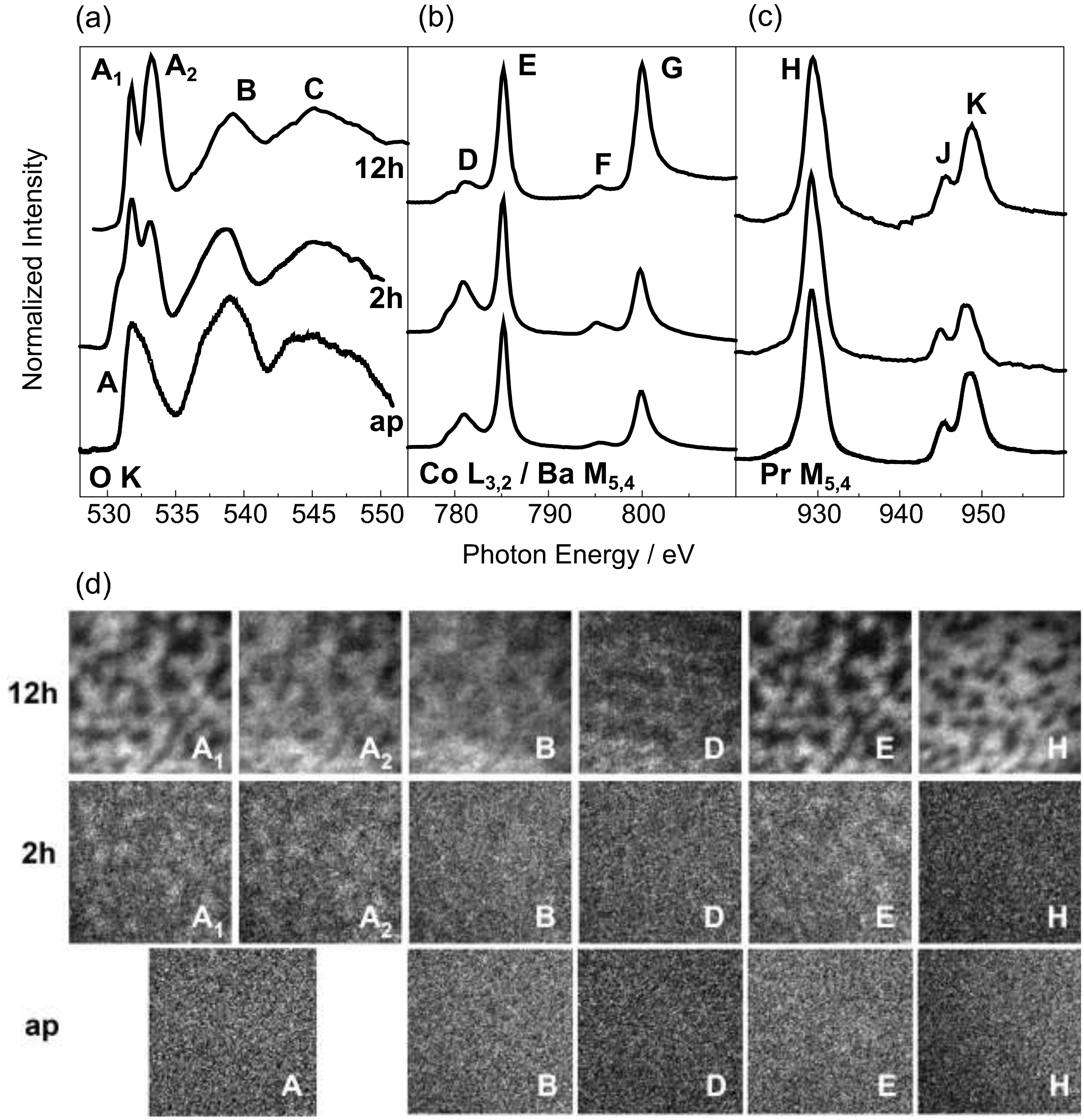

Figure 1: Spatially averaged XAS spectra for PBCO samples ‘ap’, ‘2h’ and ‘12h’shifted upwards for clarity at (a) Oxygen K-edge; (b) Cobalt $L_{3,2}$- and Barium $M_{5,4}$-edges and (c) Praseodymium $M_{5,4}$-edges. Spectra were obtained by averaging the pixel intensity of all pixels in the FoV of the raw PEEM images. Details of the sample treatment, energy resolution and the number of pixels analyzed are given in Table S1 of the supporting information. (d) 180 × 180 pixels sections (3.2 × 3.2 μm^2) of the PEEM images for photon energies corresponding to the resonant features (denoted A–K) related to XAS transitions in (a)–(c).

Mark	Edge	Transition to	Energy / eV
A	O K	O2p–Co3d	532.0
A_1	O K	O2p–Co3d (t_{2g})*	531.8
A_2	O K	O2p–Co3d (e_g)*	533.2
B	O K	O2p–Ba/Pr5d	539.2
C	O K	O2p–Co4sp	545.2
D	Co L_3	Co3$d_{3/2}$	781.2
E	Ba M_5	Ba4$f_{5/2}$	785.0
F	Co L_2	Co3$d_{1/2}$	795.6
G	Ba M_4	Ba4$f_{3/2}$	799.8
H	Pr M_5	Pr4$f_{5/2}$	930.0
J, K	Pr M_4	Pr4$f_{3/2}$	945.8 / 948.8

Table 1: Spectral feature assignments. A_1 and A_2 are denominated t_{2g} and e_g assuming low spin configuration for Co (see main text).

As reported earlier,[20] the as-prepared sample (lower row in Figure 1d) exhibits no surface structure resolvable by PEEM at any of the spectroscopic features A–K, corroborating that the films are spatially homogenous after deposition. Annealing the samples at 1073 K in 200 mbar of O_2, however, induces spatial inhomogeneities on a micrometer scale, which begin to be faintly visible in the PEEM images after annealing for 2h (middle row in Figure 1d) and become quite pronounced after 12h (upper row in Figure 1d). The average spectra show a concomitant evolution in their shape with annealing time: the feature A of the O-K-edge in the as-prepared sample is split after 2h into more distinctly separated features (A_1 and A_2) with a leading shoulder at lower energies. Features A_1 and A_2 become even more defined after 12h.

The initial shape of the O-K-edge corresponds well to that found for the end member $PrCoO_3$. [24] Here, feature A is dominated by the O2p–Co3d hybridized states forming t_{2g} and e_g states through the octahedral coordination, which, however, cannot be resolved spectroscopically.[25]

As Co-$L_{3,2}$- and Ba-$M_{5,4}$-edges are serendipitously very close in energy (but not close enough to overlap), a direct comparison between the white line intensities, D and E, respectively, already points toward cationic rearrangements having taken place: the Co/Ba ratio drops significantly after 12h of annealing, which hints at segregation of alkaline earth elements to the surface. The overall shapes of the Ba and Co spectra are conserved, the latter pointing towards no involvement of Co derived states in any redox processes in line with previous reports.[9] Similarly, the Pr edge does not show any appreciable changes.

The most appreciable changes are found in the O-K-edge: for the 'ap' sample, distinct peaks for the t_{2g} and e_g states are not readily made out, which is typical for the cobaltites.[26] In contrast, samples '2h' and '12h' show a clear separation into two peaks A_1 and A_2, which we tentatively assign to the t_{2g} and e_g states, respectively. The two peaks are separated by 1.8 eV, a value quite common of the octahedral field splitting.[27] The assignment assumes a low spin state of the hybridized Co d^6 configuration, indicating a spin state transition through oxidation.[28] The oxidation process could also invoke a transition from a metallic-like behavior to localized electrons, which has been found for the $La_xSr_{1-x}CoO_3$ solid solution series at $x \sim 0.2$.[26] The transition to localized electrons would explain the shape of the O-K-edge of the annealed samples resembling that of a ferrite.[27] Additionally, the '2h'-sample exhibits a shoulder at the low energy flank, indicating lifting of degeneracy of the t_{2g} electronic states induced by distortion of the octahedral symmetry. Breaking of this symmetry can occur through A-site or oxygen vacancy ordering, which has been observed in double perovskites.[29,30] Alternatively, it could be considered a mixture of the 'ap' and '12h' states, for example, through incomplete oxidation leading to phase separation. The incomplete oxidation is, however, incompatible with the spatial distribution explained below. Even without a detailed analysis of the spectra, it is already observable that annealing, even for short times, considerably changes the surface electronic structure. Furthermore, the peak ratio of D (Co L_3) to E (Ba M_5) is larger for the untreated 'ap' sample compared to the '2h' and '12h' samples.

To summarize, evolution of the spatially averaged spectra with annealing time shows that even comparably short exposure to post-deposition annealing treatment in oxidizing conditions induces changes in the surface chemistry beyond simple oxidation of the perovskite. As the observed process likely involves cation movement, which is considered slow at these temperatures,[31] it is imperative for an educated discussion of the oxidation process to identify any spatial inhomogeneity.

Evolution of spatial inhomogeneity with annealing time

Inspecting the PEEM images at distinct energies corresponding to characteristic electronic transitions, as listed in Table 1, reveals spatial intensity variations (see Figure 1d). It is evident that the previously homogenous sample surface shows inhomogeneities after 2h of annealing. For both the '2h' and the '12h' samples, we find that dark and bright areas in the PEEM images correlate with spectral variations in the pixel-by-pixel spectra. To associate the extent of the inhomogeneities with electronic transitions, we used PCA-treated PEEM images, which has been proven to identify even small local spectral changes.[32]. Figure 2 shows the PCA images for the '12h' sample. Not apparent in the original raw PEEM images (Figure 1d, top row) but obvious in the PCA images (Figure 2), the spectral data originate from three rather than from two domains: two domains correspond to bright, respectively dark, surface features in the raw PEEM image at A_1. The third domain is the dominant contrast in the PCA images at A_2 and B. Hence, this domain is closely related to the oxygen e_g resonance and the Ba/Pr5d-O2p hybridized states and it seems to separate the bright and dark domains. A closer inspection of the PCA images E and H (G and K are omitted for clarity, as they show the same information) indicates that high-intensity areas of the Ba and Pr PCA images seem to overlap. The bottom right panel of Figure 2 shows the sum images for E and H. Obviously, the bright border regions of the sum images correspond to regions of highest intensity in the PCA image at A_2. Hence, the bright border regions of high Ba and Pr content are where the O e_g signal is largest.

The PCA images for the '2h' sample are shown in Figure S5 of the supporting information and shall only be discussed briefly here: after 2h annealing at 1073 K in 200 mbar of O_2, the PBCO sample exhibits local contrast variations at the resonant features A_1, A_2 (O-K-Edge), D and E (Co-L- and Ba-M-edge, respectively). At the Pr-M-edge (H), the '2h' sample exhibits no pronounced lateral structures, appearing almost homogeneous.

The PCA reveals coincidences of inhomogeneities in spectral contributions of the different chemical constituents, which is especially visible in the '12h' sample. The expected oxidation would manifest in intensity variations of the t_{2g} feature A_1, as it indicates the hole concentration on the lowest unoccupied state (in a semiconductor picture). In Figure 2 it thus becomes apparent that the degree of oxidation is, indeed, inhomogeneous. Additionally, the e_g signal, whose occupation should be independent of oxidation, also shows inhomogeneities, which, in their general shape, are similar to the t_{2g} distribution, but with an intensity enhancement at the boundaries. The distribution of feature E (Ba) closely resembles that of A_2 (e_g), albeit with no obvious intensity enhancement at the boundaries. The H (Pr) distribution is complimentary to A_1 (t_{2g}). Furthermore, feature D (Co) distribution seems to be complimentary to E (Ba). The boundary phase visible in A_2 (e_g) is also visible when E (Ba) and H (Pr) are added (lower right panel in Figure 2): the bright boundaries as formed by the superposition of the images at features E and H resemble the high-intensity areas at the feature A_2. This indicates a well-ordered parent phase. Pr and Ba are both present where the e_g signature is most intense, e_g being a measure of covalency or constructive O2p–Co3d overlap,[32] which is corroborated by the boundary phase showing up in the Ba/Pr5d-O2p region.

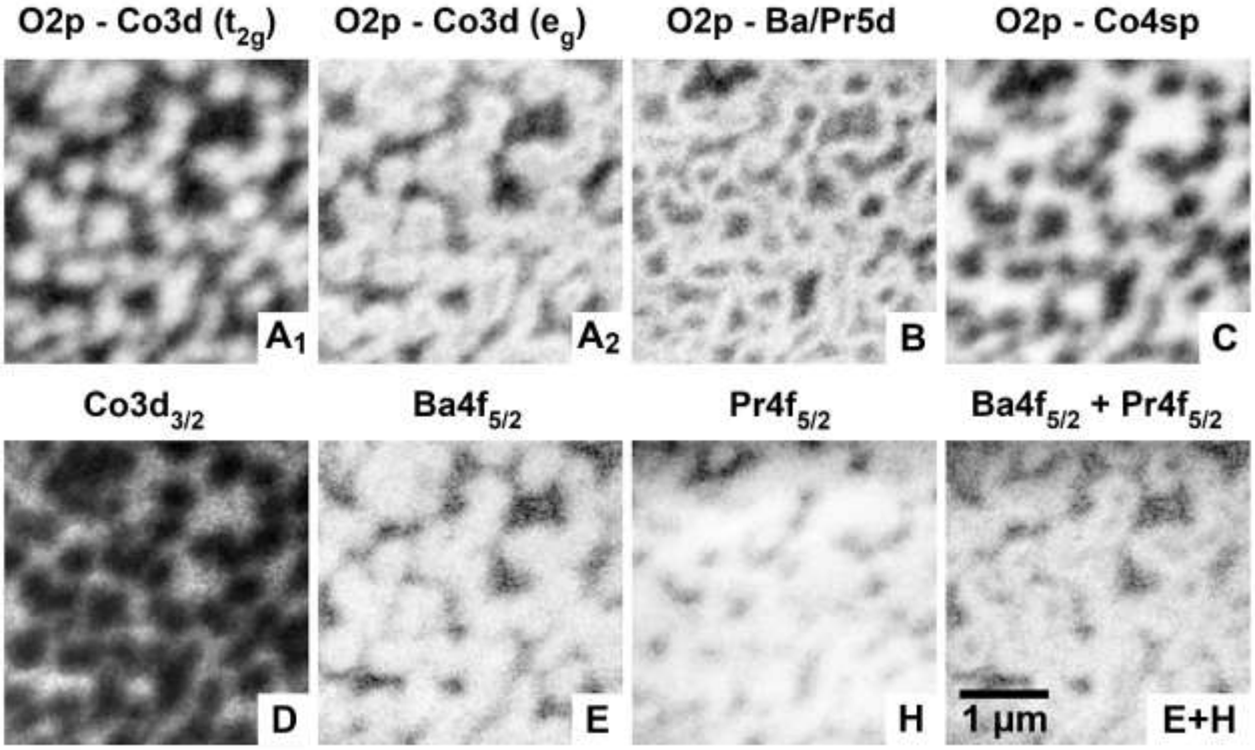

Figure 2: PCA images of $Pr_{0.5}Ba_{0.5}CoO_{3-\delta}$ annealed at 1073 K for 12 h prior to the XAS measurement (sample '12h') at various photon energies of interest as marked in Figure 1 and Table 1. In the lower right image, E+H denotes the sum of PCA images at features E and H with rescaled contrast. The overlap regions of high Ba and high Pr resemble the high-intensity border regions at resonant features A_2 and B. The scale bar applies to all images. Corresponding images for the '2h' sample are given in Figure S5 of the supporting information.

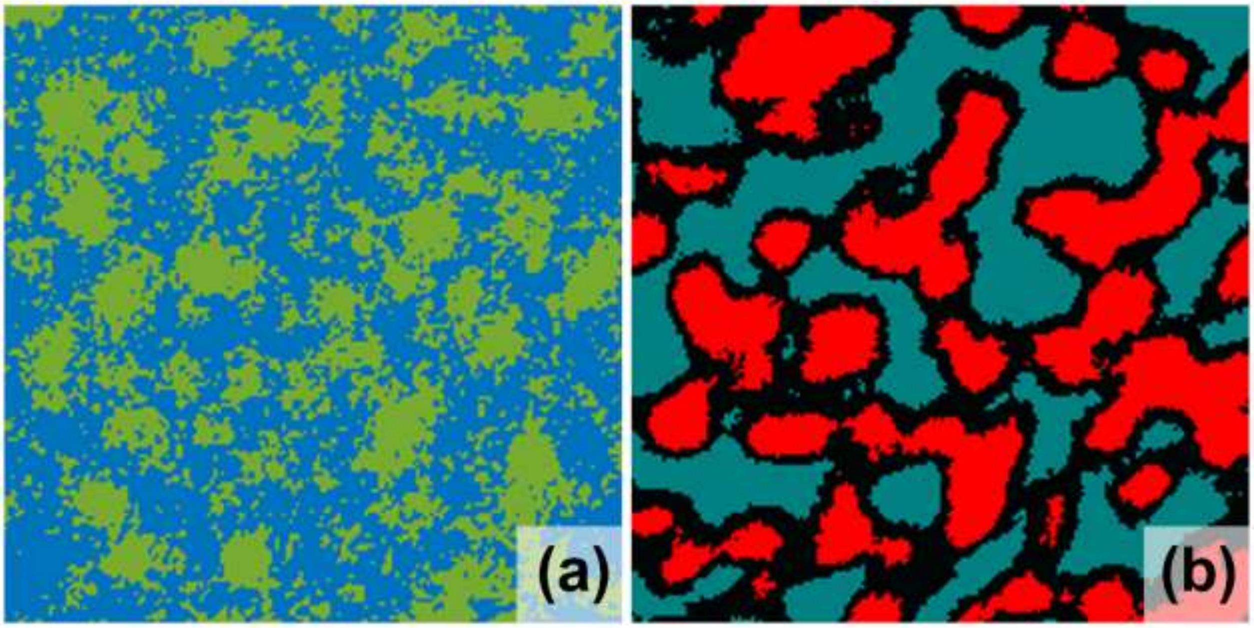

Figure 3: Cluster images as obtained from o-NNMF illustrating the different domains for (a) sample '2h' and (b) sample '12h' in a false-color display. The cluster images define areas of highest spectral similarity, i.e. regions of interest where spectral data is averaged to determine the mean spectra for the different domains, as presented in Figure 4. (For technical details on the cluster analysis see [22,23]).

In order to determine the mean spectra in the different domains of samples '2h' and '12h', we first define regions of interest where spectra are similar and supposedly belong to the same phase. For this purpose, we make use of o-NNMF as introduced in Ref 22 (for more technical details we refer to Ref. 23). Figures 3a and b show the cluster regions as determined for samples '2h' and '12h', respectively. For sample '2h', the green and blue clusters correspond to areas with high, respectively low, intensity in the PCA images in Figure S5 of the supplement. For sample '12h', the black cluster corresponds to areas with high intensity in the Ba/Pr5d-O2p resonances, i.e. feature B (Figure 2a). The bright red cluster is correlated with A_1 (t_{2g}) and E, G (Ba). Finally, the cyan cluster corresponds to features C, and D and F (Co4sp-O2p, and Co), as well as all Pr spectral features H and K. The different clusters (red, cyan, black ('12h'), respectively green, blue ('2h')) are defined as ROIs where the spectra are averaged. The number of clusters is chosen according to the minimum number of principal components that are sufficient to describe a spectrum at each pixel (see also Figure S3 of the supplement), hinting that at least three distinct phases coexist, a plausible scenario as we will explain later. We have checked for the existence of more than three phases, i.e. more than three clusters. More clusters could be used to provide finer granularity in the processes observed, however those are within the error margins of the presented data set. The corresponding mean spectra are presented in Figure 4.

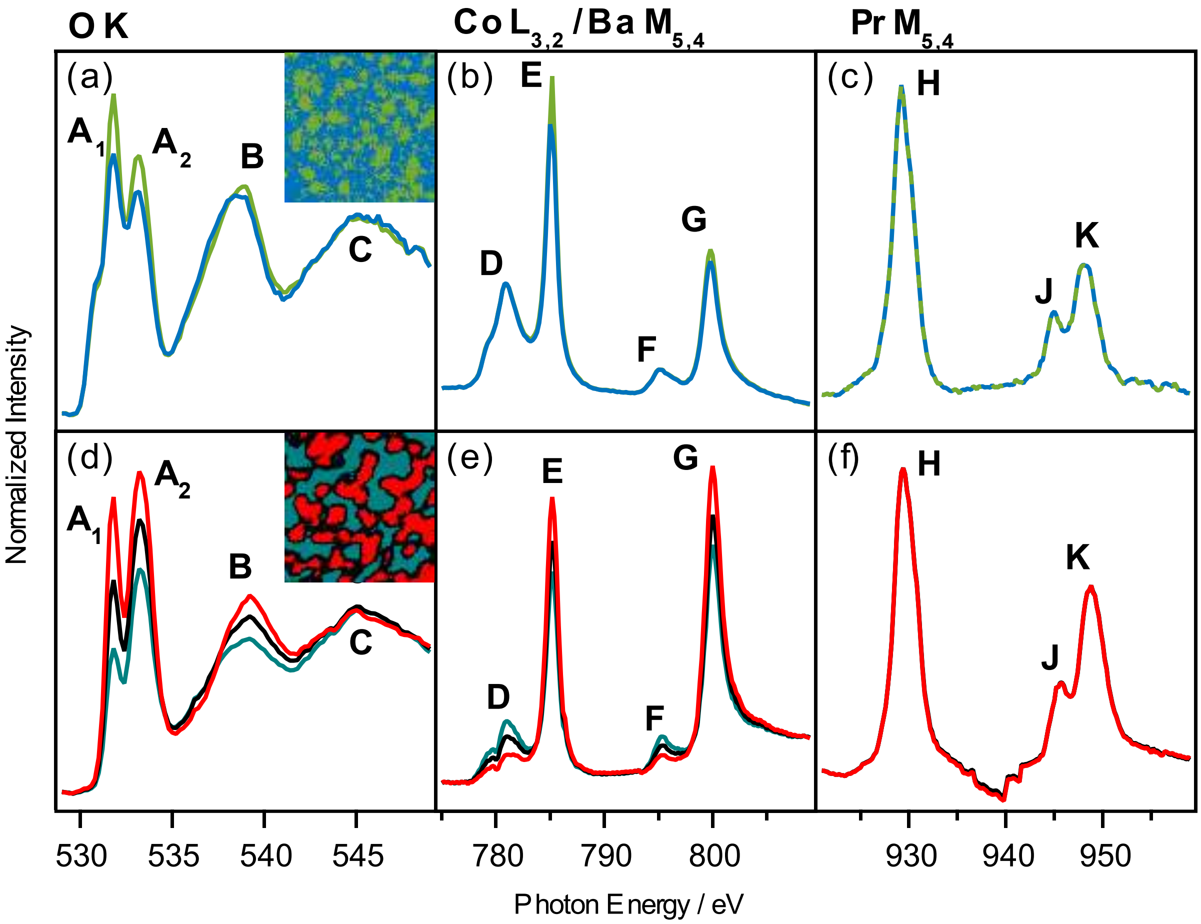

Figure 4: Mean spectra determined as the average of all spectra in the colored ROIs illustrated in Figure 3 for samples '2h' and '12h'. Details of normalization procedures are given in the supporting information.

From bulk thermodynamics, Suntsov *et al.*[30] have shown that PBCO adopts a stable perovskite phase across a wide range of temperatures and oxygen partial pressures, including the conditions of the annealing experiments here. Even if ordering phenomena of either cations or vacancies may occur,[20,33] no severe changes in chemistry and a resulting decomposition is expected, as found for other cobaltites, such as BSCF.[11] Additionally, the cubic modifications of cobaltites are, in general, stabilized towards higher oxygen partial pressures,[34,35] making a decomposition in an oxidation experiment as in this work unlikely.

The lateral distribution of the phases found in the PCA cluster images shown in Figure 3 and their evolution with annealing time now give us some indication of the process that is observed here. Annealing for 2 hours resulted in quite obvious changes in the spectra from the as-prepared state (compare bottom and center spectra in Figure 1a). Especially, the 2h O-K-edge shows a closer resemblance to the '12h' sample, but with less pronounced lateral inhomogeneities. This indicates that the oxidation process—a process involving mobile oxygen and electronic species—is much faster than any chemical rearrangement involving the movement of cations, such as A-site unmixing. Furthermore, this is compatible with the observation that miscibility gaps in complex perovskite solid solutions are highly pO_2 dependent.[35]

The lateral distribution of the '2h' sample (Figure 3a), though noisy, does show some resemblance to surface precipitation, as is observed for thin films of other alkaline earth containing perovskites when exposed to high T and pO_2.[36] Though the pattern would be compatible with a nucleation and growth mechanism, the spectra (shown in Figures 4a-c) of either species are too similar to suggest a precipitated secondary phase. Examining the spectra of each cluster in more detail, the O-K-edge (Figure 4a) only shows a variation in the strongly localized resonances A_1 and A_2 (with the pre-edge feature staying the same), which are the Co3d–O2p derived electronic states. As both occupations change concomitantly, a difference in hole concentration (or degree of oxidation) can be ruled out. Together with the varying intensity of the Co signal (D in Figure 4b), one can deduce that subtle rearrangements in the octahedral CoO_6 manifold might cause the inhomogeneities as highlighted in Figure 3a. In fact, tilting of the octahedra, as is ubiquitous in these compounds,[37] will cause a reduced overlap of the O2p and Co3d orbitals, which decreases covalency.[38] This will decrease the density of states of the hybridized orbitals visible as a decrease of the spectral signature A_1/A_2 in Figure 4a from green to blue and as an increased white line intensity (D) of the Co-L_3-edge.[39] Feature B in the O-K-edge (the Pr/Ba5d-O2p electronic states) and both Ba- and Pr-M-edges (Figure 4c) showing no difference throughout these domains further corroborate the idea that only a subtle rearrangement of the O sublattice is causing the inhomogeneities here, with no cation movement, necessary for a decomposition reaction, involved.

Turning to the '12h' sample, the overall shape of the O-K-edge (Figure 4d) is preserved from '2h', with the pre-edge absent and the weight of A_1 and A_2 reversed. It is important to point to the B region, where changes in the spectral weight are observed: these are caused by changes in the Pr/Ba ratio, similarly to La/Sr.[27] Additionally, the change of the Co/Ba ratio (Figure 4e) and the Pr intensity (Figure 4f) make a strong point for cationic rearrangements taking place. The spatial inhomogeneity, as shown in Figure 3b, is now incompatible with a nucleation and growth mechanism but rather has a close resemblance to a Cahn-Hilliard spinodal decomposition,[40] similar to what was found recently for spinel $Co_xFe_{3-x}O_4$ thin films.[41] The fact that now three principal components are necessary to describe the data for the '12h' sample further confirms this hypothesis, as diffusion occurs in both directions from a parent phase which manifests itself in the occurrence of a boundary region (black in Fig. 3b). From a chemist's point of view, the spectral evolution is compatible with an A-site unmixing, in its simplest and complete form described by

$$\left(\frac{\delta(\mathrm{PB})}{2}-\frac{\delta(\mathrm{B})}{4}-\frac{\delta(\mathrm{P})}{4}\right)\mathrm{O_2}+\mathrm{Pr_{0.5}Ba_{0.5}CoO_{3-\delta(PB)}}$$

$$\rightarrow\frac{1}{2}\mathrm{PrCoO_{3-\delta(P)}}+\frac{1}{2}\mathrm{BaCoO_{3-\delta(B)}}$$

where (P), (B) and (PB) denote the Pr-rich phase, Ba-rich phase and mixed phase, respectively.

As we observe from the ‘2h’ data, the oxidation process (i.e. changes on the oxygen sublattice) takes place at a different time scale than the cation rearrangement observed in the ‘12h’ case. This, again, makes a Cahn-Hilliard-type decomposition plausible, as it describes unmixing of compositions where species of two vastly different diffusivities are partaking. Here, the two species are likely to be identified with oxygen and the A-site cations, whose diffusivities in perovskites at temperatures in question differ by four orders of magnitude.[42,43]

Conclusion

To summarize, annealing of PLD deposited thin films of multi-component oxides such as PBCO at operating and processing conditions of solid-state electrochemical devices induces surface decomposition processes at the sub micrometer scale, similar to those of Cahn-Hilliard-type, even at annealing times as short as 12h. These rearrangements are probably confined to the surface, as a) bulk thermodynamic data suggests the material to be stable in these conditions, and b) a Cahn-Hilliard-type mechanism excludes the typical nucleation and growth mechanism observed for decompositions that are found to happen when the material is annealed in its miscibility gap. Disregarding the exact mechanism and the driving force of the decomposition, from the spectral analysis, it is evident that the electronic structure is severely impacted. Especially one of the proposed descriptors—the e_g electron—appears to be elusive, as its spectroscopic signature’s intensity shows significant lateral variation. Quantifying this descriptor with an averaging technique implies that the proposed catalytic efficacy follows this average, which may not be correct. Furthermore, it shows that designing a material has its limitation: the descriptor evolves significantly with high temperature processing or application and much more so at the surface than is expected from the bulk. This should have a profound impact on catalysis research: even determining these descriptors with spatially averaging techniques should now be questioned, and it should be understood that phenomena observed in our study need to be considered.

Generally speaking, these decomposition pathways do not have to be limited to thin films, but could also occur in technologically relevant morphologies, such as particles. Christensen et al.[44] showed that there is a unique scaling relation between mean structure size of the separated phase and particle size. Given that our structure size is on the 100 nm scale, choosing smaller particle sizes (which is preferred in any case to maximize surface area) might be a way to alleviate the issue. There is a lower particle size limit beyond which phase separation vanishes,[44] but it is likely beyond any technologically relevant (or achievable) particle size for oxide electrocatalysts. However, even if the phase separations we observe could be completely prevented by a proper choice of particle size, this would mean that particles and thin films are not comparable, and thus the former should not be used as model systems for the latter.

Having detailed knowledge of such kind of phenomena and their underlying driving forces and mechanisms may even open up design strategies for complex catalyst systems: preordaining surface rearrangements to form nanoscale composite structures of synergizing catalyst materials that are chemically less complex than the initial phase can become a valid strategy to find catalyst materials of unprecedented performance and stability. Furthermore, boundary phases now present in significant abundance may give access to properties not achievable from monolithic materials. All of this, however, does necessitate analytical methods with simultaneous chemical and lateral sensitivity to resolve in situ formation of novel catalyst phases.

Supporting Information

Table S1: Overview of annealing conditions and details on spectromicroscopic measurements

Figure S1: Full field of view PEEM images of the 12h annealed samples at spectral signatures listed in Table 1

Figure S2: Full field of view PEEM images of the 2h and as prepared samples at spectral signatures listed in Table 1

Figure S3: Principal component loadings of the first three principal components for all samples

Figure S4: Comparison between PEEM images and PCA loading mapping images, respectively, PCA images at spectral signatures A, A_1, and A_2 for all samples.

Figure S5: PCA images of the 2h annealed sample at spectral signatures listed in Table 1

Figure S6: Full field of view PEEM image reconstruction for the 12h annealed sample based on the first relevant principal components.

Figure S7: Full field of view PEEM image reconstruction for the 2h annealed sample based on the first relevant principal components.

Details on the normalization procedure of the spectra in Fig. 4

Raw TIFF-files for all images are available as download.

Acknowledgements

The authors thank the Helmholtz Zentrum für Materialien und Energie Berlin, Germany and ELETTRA sincrotrone Trieste, Italy for the allocation of synchrotron radiation beamtime. Beamtime support by J. Hackl, S. Nemšák and M. Andrä is gratefully acknowledged. DNM gratefully acknowledges support by the Jülich Joint Redox Lab (JJRL) and financial support through the German Science Foundation (DFG) in the frame of the priority program "Manipulation of matter controlled by electric and magnetic field: Towards novel synthesis and processing routes of inorganic materials" (SPP 1959)

References

(1) Nørskov, J.; Rossmeisl, J.; Logadottir, A.; Lindqvist, L.; Kitchin, J.; Bligaard, T.; Jonsson, H. Origin of the Overpotential for Oxygen Reduction at a Fuel-Cell Cathode. *J. Phys. Chem. B* **2004**, *108* (46), 17886–17892. https://doi.org/10.1021/jp047349j.

(2) Stamenkovic, V. R.; Mun, B. S.; Arenz, M.; Mayrhofer, K. J. J.; Lucas, C. A; Wang, G.; Ross, P. N.; Markovic, N. M. Trends in Electrocatalysis on Extended and Nanoscale Pt-Bimetallic Alloy Surfaces. *Nat. Mater.* **2007**, *6* (3), 241–247. https://doi.org/10.1038/nmat1840.

(3) Greeley, J.; Stephens, I. E. L.; Bondarenko, A. S.; Johansson, T. P.; Hansen, H. A.; Jaramillo, T. F.; Rossmeisl, J.; Chorkendorff, I.; Nørskov, J. K. Alloys of Platinum and Early Transition Metals as Oxygen Reduction Electrocatalysts. *Nat. Chem.* **2009**, *1* (7), 552–556. https://doi.org/10.1038/nchem.367.

(4) Suntivich, J.; Gasteiger, H. a; Yabuuchi, N.; Nakanishi, H.; Goodenough, J. B.; Shao-Horn, Y. Design Principles for Oxygen-Reduction Activity on Perovskite Oxide Catalysts for Fuel Cells and Metal-Air Batteries. *Nat. Chem.* **2011**, *3* (7), 546–550. https://doi.org/10.1038/nchem.1069.

(5) Richter, J.; Holtappels, P.; Graule, T.; Nakamura, T.; Gauckler, L. J. Materials Design for Perovskite SOFC Cathodes. *Monatshefte fur Chemie* **2009**, *140* (9), 985–999. https://doi.org/10.1007/s00706-009-0153-3.

(6) Jacobs, R.; Mayeshiba, T.; Booske, J.; Morgan, D. Material Discovery and Design Principles for Stable, High Activity Perovskite Cathodes for Solid Oxide Fuel Cells. *Adv. Energy Mater.* **2018**, *8* (11), 1–12. https://doi.org/10.1002/aenm.201702708.

(7) Suntivich, J.; May, K. J.; Gasteiger, H. A; Goodenough, J. B.; Shao-Horn, Y. A Perovskite Oxide Optimized for Oxygen Evolution Catalysis from Molecular Orbital Principles. *Science* **2011**, *334* (6061), 1383–1385. https://doi.org/10.1126/science.1212858.

(8) Hong, W. T.; Welsch, R. E.; Shao-Horn, Y. Descriptors of Oxygen-Evolution Activity for Oxides: A Statistical Evaluation. *J. Phys. Chem. C* **2016**, *120* (1), 78–86. https://doi.org/10.1021/acs.jpcc.5b10071.

(9) Mueller, D. N.; Machala, M. L.; Bluhm, H.; Chueh, W. C. Redox Activity of Surface Oxygen Anions in Oxygen-Deficient Perovskite Oxides during Electrochemical Reactions. *Nat. Commun.* **2015**, *6*, 6097. https://doi.org/10.1038/ncomms7097.

(10) Antipin, D.; Risch, M. Trends of Epitaxial Perovskite Oxide Films Catalyzing the Oxygen Evolution Reaction in Alkaline Media. *J. Phys. Energy* **2020**, *2* (3), 032003. https://doi.org/10.1088/2515-7655/ab812f.

(11) Mueller, D. N.; Souza, R. A. De; Weirich, T. E.; Roehrens, D.; Mayer, J.; Martin, M. A Kinetic Study of the Decomposition of the Cubic Perovskite-Type Oxide $Ba_xSr_{1-X}Co_{0.8}Fe_{0.2}O_{3-Delta}$ (BSCF) (X=0.1 and 0.5). *Phys. Chem. Chem. Phys.* **2010**, *12* (35), 10320–10328.

(12) Lee, Y.-L.; Kleis, J.; Rossmeisl, J.; Shao-Horn, Y.; Morgan, D. Prediction of Solid Oxide Fuel Cell Cathode Activity with First-Principles Descriptors. *Energy Environ. Sci.* **2011**, *4* (10), 3966. https://doi.org/10.1039/c1ee02032c.

(13) Crumlin, E. J.; Mutoro, E.; Liu, Z.; Grass, M. E.; Biegalski, M. D.; Lee, Y.-L.; Morgan, D.; Christen, H. M.; Bluhm, H.; Shao-Horn, Y. Surface Strontium Enrichment on Highly Active Perovskites for Oxygen Electrocatalysis in Solid Oxide Fuel Cells. *Energy Environ. Sci.* **2012**, *5* (3), 6081. https://doi.org/10.1039/c2ee03397f.

(14) Keeble, D. J.; Wicklein, S.; Dittmann, R.; Ravelli, L.; MacKie, R. A.; Egger, W. Identification of A- and B-Site Cation Vacancy Defects in Perovskite Oxide Thin Films. *Phys. Rev. Lett.* **2010**, *105* (22), 3–6. https://doi.org/10.1103/PhysRevLett.105.226102.

(15) Salmeron, M. From Surfaces to Interfaces: Ambient Pressure XPS and Beyond. *Top. Catal.* **2018**, *61* (20), 2044–2051. https://doi.org/10.1007/s11244-018-1069-0.

(16) Duchoň, T.; Hackl, J.; Mueller, D. N.; Kullgren, J.; Du, D.; Senanayake, S. D.; Mouls, C.; Gottlob, D. M.; Khan, M. I.; Cramm, S.; *et al*. Establishing Structure-Sensitivity of Ceria Reducibility: Real-Time Observations of Surface-Hydrogen Interactions. *J. Mater. Chem. A* **2020**, *8* (11), 5501–5507. https://doi.org/10.1039/c9ta11784a.

(17) Tarancon, A.; Burriel, M.; Santiso, J.; Skinner, S. J.; Kilner, J. A. Advances in Layered Oxide Cathodes for Intermediate Temperature Solid Oxide Fuel Cells. *J. Mater. Chem.* **2010**, *20* (19), 3799–3813.

(18) Bick, D. S.; Griesche, J. D.; Schneller, T.; Staikov, G.; Waser, R.; Valov, I. $Pr_xBa_{1-x}CoO_3$ Oxide

Electrodes for Oxygen Evolution Reaction in Alkaline Solutions by Chemical Solution Deposition. *J. Electrochem. Soc.* **2016**, *163* (3), F166–F170. https://doi.org/10.1149/2.0311603jes.

(19) Grimaud, A.; May, K. J.; Carlton, C. E.; Lee, Y.-L.; Risch, M.; Hong, W. T.; Zhou, J.; Shao-Horn, Y. Double Perovskites as a Family of Highly Active Catalysts for Oxygen Evolution in Alkaline Solution. *Nat. Commun.* **2013**, *4*. https://doi.org/10.1038/ncomms3439.

(20) Gunkel, F.; Jin, L.; Mueller, D. N.; Hausner, C.; Bick, D. S.; Jia, C.; Schneller, T.; Valov, I.; Waser, R.; Dittmann, R. Ordering and Phase Control in Epitaxial Double-Perovskite Catalysts for the Oxygen Evolution Reaction. *ACS Catal.* **2017**, *7*, 7029–7037.

(21) Joliffe, I. T. *Principal Component Analysis*; Springer: New York, NY, 1986.

(22) Mirzal, A. Orthogonal Nonnegative Matrix Factorization for Blind Image Separation. In *Advances in Visual Informatics*; Zaman, H. B., Robinson, P., Olivier, P., Shih, T. K., Velastin, S., Eds.; Springer International Publishing: Cham, 2013; pp 25–35.

(23) Giesen, M.; Jugovac, M.; Zamborlini, G.; Feyer, V.; Gunkel, F.; Mueller, D. N. Principal Component Analysis: Reveal Camouflaged Information in x-Ray Absorption Spectroscopy Photoemission Electron Microscopy of Complex Thin Oxide Films. *Thin Solid Films* **2018**, *665* (December 2017), 75–84. https://doi.org/10.1016/j.tsf.2018.09.010.

(24) Scherrer, B.; Harvey, A. S.; Tanasescu, S.; Teodorescu, F.; Botea, A.; Conder, K.; Grundy, A. N.; Martynczuk, J.; Gauckler, L. J. Correlation between Electrical Properties and Thermodynamic Stability of $ACoO_{(3\text{-}Delta)}$ Perovskites (A = La, Pr, Nd, Sm, Gd). *Phys. Rev. B Condens. Matter* **2011**, *84* (8), 85113/1-9.

(25) Toulemonde, O.; N'Guyen, N.; Studer, F.; Traverse, A. Spin State Transition in LaCoO3 with Temperature or Strontium Doping as Seen by XAS. *J. Solid State Chem.* **2001**, *158* (2), 208–217. https://doi.org/10.1006/jssc.2001.9094.

(26) And; Y. Lee, S. M.; Zheng, H.; Mitchell, J. F.; Freeland, J. W.; Harmon, B. N.; Bridges, F.; Medling, S.; Lee, Y.; Zheng, H. *et al.* Evolution of Magnetic Oxygen States in Sr-Doped $LaCoO_3$. *Phys. Rev. Lett.* **2012**, *109* (15), 157204. https://doi.org/10.1103/PhysRevLett.109.157204.

(27) Abbate, M.; de Groot, F. M. F.; Fuggle, J. C.; Strebel, O.; Lopez, F.; Domke, M.; Kaindl, G.; Sawatzky, G. A.; Takano, M.; Takeda, *et al*. Controlled-Valence of $La_{1\text{-}X}Sr_xFeO_3$ and $La_{1\text{-}X}Sr_xMnO_3$ Studied by Soft x-Ray Absorption Spectroscopy. *Phys. Rev. B* **1992**, *46* (8), 4511–4519. https://doi.org/10.1103/PhysRevB.46.4511.

(28) Herrero-Martin, J.; Garcia-Munoz, J. L.; Kvashnina, K.; Gallo, E.; Subias, G.; Alonso, J. A.; Baron-Gonzalez, A. J. Spin-State Transition in $Pr_{0.5}Ca_{0.5}CoO_3$ Analyzed by x-Ray Absorption and Emission Spectroscopies. *Phys. Rev. B - Condens. Matter Mater. Phys.* **2012**, *86* (12), 125106/1-6. https://doi.org/10.1103/PhysRevB.86.125106.

(29) Cox-Galhotra, R. A.; Huq, A.; Hodges, J. P.; Yu, C.; Wang, X.; Gong, W.; Jacobson, A. J.; McIntosh, S. An In-Situ Neutron Diffraction Study of the Crystal Structure of $PrBaCo_2O_{5+d}$

at High Temperature and Controlled Oxygen Partial Pressure. *Solid State Ionics* **2013**, *249–250*, 34–40. https://doi.org/10.1016/j.ssi.2013.07.017.

(30) Suntsov, A. Y.; Leonidov, I. A.; Patrakeev, M. V.; Kozhevnikov, V. L. Defect Formation in Double Perovskites $PrBaCo_{2-X}Cu_XO_{5+\delta}$ at Elevated Temperatures. *Solid State Ionics* **2015**, *274*, 17–23. https://doi.org/10.1016/j.ssi.2015.02.004.

(31) Kubicek, M.; Limbeck, A.; Frömling, T.; Hutter, H.; Fleig, J. Relationship between Cation Segregation and the Electrochemical Oxygen Reduction Kinetics of $La_{0.6}Sr_{0.4}CoO_{3-\delta}$ Thin Film Electrodes. *J. Electrochem. Soc.* **2011**, *158* (6), B727. https://doi.org/10.1149/1.3581114.

(32) Stadler, D.; Mueller, D. N.; Brede, T.; Duchoň, T.; Fischer, T.; Sarkar, A.; Giesen, M.; Schneider, C. M.; Volkert, C. A.; Mathur, S. Magnetic Field-Assisted Chemical Vapor Deposition of Iron Oxide Thin Films: Influence of Field-Matter Interactions on Phase Composition and Morphology. *J. Phys. Chem. Lett.* **2019**, *10* (20), 6253–6259. https://doi.org/10.1021/acs.jpclett.9b02381.

(33) Frontera, C.; Caneiro, A.; Carrillo, A.; Oro-Sole, J.; Garcia-Munoz, J. Tailoring Oxygen Content on $PrBaCo_2O_{5+delta}$ Layered Cobaltites. *Chem. Mater.* **2005**, *17* (22), 5439–5445. https://doi.org/10.1021/cm051148q.

(34) Kuhn, M.; Fukuda, Y.; Hashimoto, S.; Sato, K.; Yashiro, K.; Mizusaki, J. Oxygen Nonstoichiometry and Thermo-Chemical Stability of Perovskite-Type $La_{0.6}Sr_{0.4}Co_{1-Y}FeyO_{3-\delta}$ (y = 0, 0.2, 0.4, 0.5, 0.6, 0.8, 1) Materials. *J. Electrochem. Soc.* **2012**, *160* (1), F34–F42. https://doi.org/10.1149/2.050301jes.

(35) Mueller, D. N.; Souza, R. A. De; Yoo, H. I.; Martin, M. Phase Stability and Oxygen Nonstoichiometry of Highly Oxygen-Deficient Perovskite-Type Oxides: A Case Study of $(Ba,Sr)(Co,Fe)O_{3-Delta}$. *Chem. Mater.* **2012**, *24* (2), 269–274.

(36) Lee, W.; Han, J. W.; Chen, Y.; Cai, Z.; Yildiz, B. Cation Size Mismatch and Charge Interactions Drive Dopant Segregation at the Surfaces of Manganite Perovskites. *J. Am. Chem. Soc.* **2013**, *135* (21), 7909–7925. https://doi.org/10.1021/ja3125349.

(37) Glazer, A. M. The Classification of Tilted Octahedra in Perovskites. *Acta Crystallogr. Sect. B Struct. Crystallogr. Cryst. Chem.* **1972**, *28* (11), 3384–3392. https://doi.org/10.1107/S0567740872007976.

(38) Suntivich, J.; Hong, W. Estimating Hybridization of Transition Metal and Oxygen States in Perovskites from OK-Edge X-Ray Absorption Spectroscopy. *J. Phys. Chem. C* **2014**, *118*, 1856–1863.

(39) Tchougreeff, A. L.; Dronskowski, R. Nephelauxetic Effect Revisited ´. *Int. J. Quantum Chem.* **2009**, *109*, 2606–2621. https://doi.org/10.1002/qua.

(40) Cahn, J. W. Free Energy of a Nonuniform System. II. Thermodynamic Basis. *J. Chem. Phys.* **1959**, *30* (5), 1121–1124. https://doi.org/10.1063/1.1730145.

(41) Debnath, N.; Kawaguchi, T.; Kumasaka, W.; Das, H.; Shinozaki, K.; Sakamoto, N.; Suzuki,

H.; Wakiya, N. As-Grown Enhancement of Spinodal Decomposition in Spinel Cobalt Ferrite Thin Films by Dynamic Aurora Pulsed Laser Deposition. *J. Magn. Magn. Mater.* **2017**, *432*, 391–395. https://doi.org/10.1016/j.jmmm.2017.02.023.

(42) Harvey, S. P.; De Souza, R. A.; Martin, M. Diffusion of La and Mn in $Ba_{0.5}Sr_{0.5}Co_{0.8}Fe_{0.2}O_{3-\delta}$ Polycrystalline Ceramics. *Energy Environ. Sci.* **2012**, *5* (2), 5803–5813. https://doi.org/10.1039/c1ee02740a.

(43) Wang, L.; Merkle, R.; Maier, J.; Acartürk, T.; Starke, U. Oxygen Tracer Diffusion in Dense $Ba_{0.5}Sr_{0.5}Co_{0.8}Fe_{0.2}O_{3-\delta}$ Films. *Appl. Phys. Lett.* **2009**, *94* (7), 1–4. https://doi.org/10.1063/1.3085969.

(44) Christensen, A.; Stoltze, P.; Norskov, J. K. Size Dependence of Phase Separation in Small Bimetallic Clusters. *J. Phys. Condens. Matter* **1995**, *7* (6), 1047–1057. https://doi.org/10.1088/0953-8984/7/6/008.

TOC Figure